

Full Length Article

Laser-induced scanning transfer deposition of silver electrodes on glass surfaces: A green and scalable technology

R. Molina^a, M. Ertuğrul^{b,c}, Á. Larrea^c, R. Navarro^c, V. Rico^d, F. Yubero^d, A.R. González-Elipe^d, G.F. de la Fuente^c, L.A. Angurel^{c,*}

^a IQAC-CSIC, 08034 Barcelona, Spain

^b Karadeniz Technical University, 61080 Ortahisar/Trabzon, Turkey

^c INMA (CSIC-Universidad de Zaragoza), c/ María de Luna, 3, 50018 Zaragoza, Spain

^d ICMS (CSIC-Universidad de Sevilla), c/Américo Vespucio 49, 41092 Sevilla, Spain



ARTICLE INFO

Keywords:

LIRT
DBD
Laser ablation
Metallization
Glass

ABSTRACT

A pulsed laser ablation backwriting technique with high repetitive rates is implemented for the fabrication of silver coatings on glass surfaces. This method enables geometrical constraint-free deposition of metallic coatings. These exhibit sufficiently low electrical resistance to be used as electrodes in dielectric barrier discharge (DBD) plasma elements.

Ambient air deposition of metallic silver electrodes on standard glass slides is explored using a sub-ns UV laser source, combined with hybrid beam scanning methods. The green nature of the overall deposition process includes a preliminary irradiation scan to homogenise the target surface before the subsequent backwriting step. Metal transfer is achieved by combining two phenomena within a simple beam scanning process: LIRT (laser-induced reverse transfer) of silver from the target to the glass, with a partial and secondary LIFT (Laser-Induced Forward Transfer) of silver from the glass to the target.

Appropriate selection of pulse energy and pulse repetition rates, beam scanning velocities and target motion enable the growth of sufficiently thick Ag deposits on glass with the required low electrical resistivity and nearly 2D constraint-free geometry. This method avoids the use of vacuum and liquids, resulting in a cheap, facile and green methodology for the deposition of silver electrodes onto transparent substrate surfaces.

1. Introduction

Most standard coating and film deposition methods rely on the use of vacuum techniques [1] or, alternatively, on the use of liquids, whether the latter are sols [2], solvents [3] or colloidal dispersions [4]. In this regard, electroless plating [5] or vacuum-based metal deposition on glass and other substrates are common methods for many industrial and technological applications. Vacuum methods, including evaporation [6], magnetron sputtering [7], cathodic vacuum arc [8], ion plating [9], pulse laser deposition [10,11] or, more recently, atomic layer deposition [12,13] have been carried out to deposit metals on glass. A large number of laser-based direct writing techniques have also been applied to obtain metallic coatings on non-conductive substrates. Laser-direct writing [14] is a low-cost, maskless and fast fabrication technique that sinters a metal nanoparticle ink over the transparent substrate. The search for new ink compositions that allow improving the mechanical performance

of the coating over different substrates is still an open question. Laser selective metallization [15,16] makes use of irradiation treatments to locally activate a substrate surface, in order to facilitate selective metallization by electroless plating. Laser-Induced Forward Transfer (LIFT) is also a digital printing technique that takes advantage of laser pulses to project material from a donor towards a receiving substrate [17–20]. LIFT has been applied to obtain coatings from solid metal films, metal pastes or liquid inks. In another method, laser induced molten transfer [21], a laser irradiates and melts a donor foil in order to project its molten droplets with the help of induced laser shock waves. An additional alternative makes use of a laser pulse to mechanically delaminate and project a solid film with no phase change [22].

Many of these deposition methods, particularly those involving liquid procedures or vacuum technologies, present disadvantages from several points of view. These include energy and process efficiency, the requirement of vacuum, sometimes the use of expensive apparatus and

* Corresponding author.

E-mail address: angurel@unizar.es (L.A. Angurel).

<https://doi.org/10.1016/j.apsusc.2021.149673>

Received 9 January 2021; Received in revised form 18 March 2021; Accepted 25 March 2021

Available online 8 April 2021

0169-4332/© 2021 The Author(s).

Published by Elsevier B.V. This is an open access article under the CC BY-NC-ND license

(<http://creativecommons.org/licenses/by-nc-nd/4.0/>).

limited scalability, and often a high environmental cost. It seems thus desirable to develop methods that avoid, at least for the deposition of given materials, some of the mentioned disadvantages. If such methods are based on dry processes and do not require vacuum, they present an additional attractive perspective, since they would help avoid the use of water or other more environmentally aggressive solvents, and would be ideal for development in the laboratory of Industry 4.0 type fabrication methods, as well as for the improvement of industrial coating and film deposition processes.

One of these potentially useful dry deposition methods on transparent substrates is the Laser-Induced Reverse Transfer (LIRT) technique presented here, also known as Laser Ablation Backwriting (LAB) [23–26]. It was initially introduced as a variant of the LIFT method [18]. One of the main advantages of the LIRT process is that it does not demand any special preparation of the donor material, opening the possibility of using readily available bulk sample targets. Several papers have reported the use of this technique to coat glass substrates with metal [18,24–29] or oxide layers, as for instance In_2O_3 layers [28]. It was observed in several cases that, at low fluence values, small uniform deposits are obtained. At high fluence values, however, the deposited material exhibits a crater-like morphology, apparently due to the preferential condensation at the cooler edges of the substrate.

This technique has been proposed as a powerful alternative for several applications. For example, the development of optical components such as optical waveguides [24–26] or diffraction gratings [30,31] has been demonstrated in recent years. According to the published literature, optical properties of these films were basically a result of the incorporation of metal nanoparticles into the outermost layer of the glass substrate [26], where a buried type waveguide structure was induced by the metal ablation process inherent to this deposition method. LIRT has also been proposed as a convenient method to modify different surface properties of glass. This has been demonstrated to achieve superhydrophilic or superhydrophobic character [32], or to improve surface biocompatibility and enhance in-vitro cell adhesion [33]. In addition, the use of LIRT processes towards decontamination of radioactive surfaces has also been demonstrated [18].

The main objective of this work was to develop a dry and simple metal electrode deposition technique for glass surfaces. A second objective included the development of a model to account for the influence of process parameters on the final microstructure and functionalities of the deposited metal layers. Adequate levels of electrical resistance and different geometries, as required for developing surface dielectric barrier discharge (DBD) demonstrators, were the prerequisites. The common DBD principle is to place an insulating (dielectric) material between metallic, good conductor finger electrodes [34]. Surface DBD actuator applications have most recently expanded to wide open technology areas, such as active control of flow over aerodynamic bodies [35], ozone synthesis and nitric oxide conversion from air [36], air disinfection to food storage [37], polymer surface modification [38] or inactivation of bacteria and endospores [39–41].

2. Experimental section

Fig. 1 shows a drawing of the apparatus used to carry out the deposition experiments. A 3 W nominal power, UV ($\lambda = 355 \text{ nm}$) 300 ps pulsed laser, emitting at pulse repetition rates ranging between 250 and 800 kHz (model PowerLine pico UV, ROFIN GmbH., Munich, Germany) was employed. A 1 mm thick flat silver sheet (Goodfellow, 99.95+%) was placed at the focal length of the Galvo Scan Head with a flat field lens ($F = 160 \text{ mm}$), producing an elliptical beam with $2a = 34 \mu\text{m}$ and $2b = 29 \mu\text{m}$ ($1/e^2$ intensity contour criteria).

The same Ag target was used for all deposition experiments. With the objective of working in all the cases with a similar surface topography, as well as to improve laser absorption, a surface preparation protocol was applied before each deposition process. The target was thus initially polished with a 1200 grade sand paper and cleaned with alcohol before

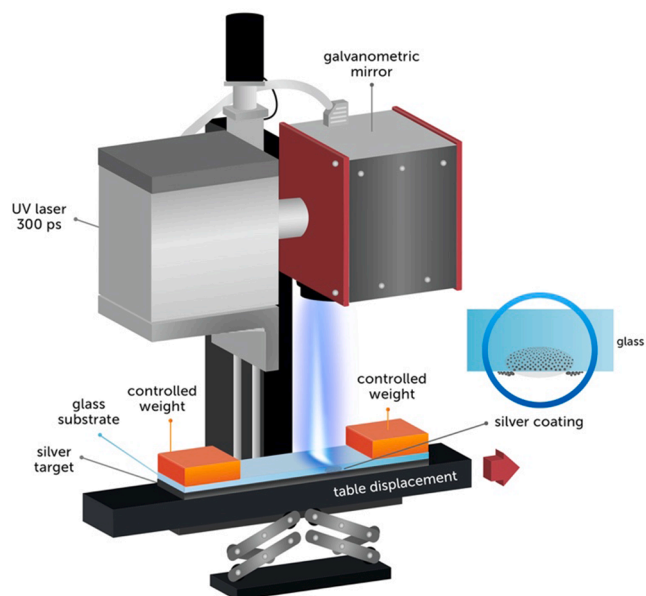


Fig. 1. Scheme of the laser source and sample disposition during the experiments. The laser system incorporates a galvanometer mirror box at the output, to enable beam scanning at the focal plane, coincident with the Ag substrate surface. A glass slide is fixed above this substrate on a precision displacement table. Simultaneous beam scanning and transverse Ag and glass slide displacement at constant rates may be combined.

the initial laser treatment was performed. The same laser source was used to scan the surface with pulse energies of $4 \mu\text{J}$ (1.73 GW/cm^2 of irradiance), repetition rates of 400 kHz and beam scan velocities $v_L = 1000 \text{ mm/s}$ and keeping a distance between adjacent scan lines of $8 \mu\text{m}$. Fig. Sup1 shows the Ag surface after this preparation step, before starting the coating process. These irradiation conditions are far above the ablation threshold, generating a sub-micrometric rough uniform surface with randomly oriented and solidified molten structures. These are joined by necking to small Ag spheres with diameters below 200 nm . In spite of the intense melting and erosion process undergone by the target surface, only metallic Ag is detected by EDS, with no appreciable oxidation, as it is presented in Fig Sup1.

A pristine glass slide (Thermo Scientific), $1 \times 25 \times 75 \text{ mm}^3$, was placed directly on top of the Ag target and secured with a sleeved brass block of 171.2 g. The latter was adjusted to fit the glass substrate perimeter and rest on its ca. 1 mm sleeve, in order to obtain reproducible pressure and distance between the glass and the silver target. A laser line-scanning process was carried out in air [42]. The pulsed laser beam moved in one direction with scanning speed v_L , describing a line formed by successive pulses, while the sample was displaced in the perpendicular direction at a given traverse speed in order to control the extent of overlap between consecutive beam scanned lines.

A wide range of laser processing parameters has been explored in the course of this investigation. The reported results correspond to those conditions providing an optimal functionality and/or those required to propose a sound model accounting for the film formation mechanism. To determine the relationship between laser pulse patterns made on the Ag target, and the final deposit observed on the glass substrate placed above it, initial experiments were carried out in which single spots in burst mode were deposited onto the glass slide substrates under different conditions, varying the number of irradiated spots and the pulse repetition rate. Single lines were also deposited using a beam scanning operation mode. Further microstructure studies were carried out on larger areas obtained with the same configuration, but using the laser line scan algorithm in order to investigate how laser pulse overlap affects the final deposit attained on the glass substrate. Pulse to pulse overlap may take place within the laser scanned line and, in an

orthogonal direction, between different laser lines.

The microstructure of the obtained deposits was studied using secondary electrons and in-lens secondary electron detectors in a Field-Emission Scanning Electron Microscope (FE-SEM, Carl Zeiss MERLIN). Chemical surface characterization was performed using Energy Dispersive X-ray Spectroscopy (EDS, INCA350 Oxford Instruments) with electron acceleration voltages of 5 kV.

Cross-sections of selected samples were analysed using Transmission Electron Microscopy. Specimen cross-section preparation was carried out with a Focused Ion Beam (FIB) in a Dual Beam FEI Helios 650 apparatus, using 30 kV Ga⁺ ions for the initial steps and 5 kV for final thinning. High-resolution STEM images were obtained using a FEI Titan 60–300 kV Cube microscope, equipped with a spherical image aberration corrector. Electron diffraction was performed in a FEI Tecnai F30 microscope.

In addition, X-ray photoelectron spectroscopy (XPS) was applied to characterize the surface chemical state of the deposits. Selected samples were introduced in the analysis chamber of a SPECS PHOIBOS-100 spectrometer and spectra recorded with the Al K α line. Binding energy (BE) scale of the spectra was referred to the C 1s peak taken at 284.5 eV for the adventitious carbon contaminating the surface of samples.

Electrical transport characteristics of the obtained coatings were determined by measuring the DC electrical resistance using a four-point probe device. These were measured on samples with 20 × 4 mm² rectangular deposits prepared by LIRT with the laser scanning direction applied along the longest side of the rectangular shaped sample, while it was moving at a constant rate in its perpendicular direction (coincident with its shortest side). Parallel to the latter direction, four terminals were placed with two current (I) injection terminals disposed at 10 mm and two central voltage (V) terminals in the centre at a distance of 3 mm.

Coating adhesion strength was evaluated using a Scotch Tape Test. A piece of scotch tape was placed on top of a rectangular Ag coating in the direction parallel to the longest side of the rectangle. The tape was smoothed to ensure good contact with the coating and removed with a single, fast motion pulling step. The process was repeated up to six times and the electrical resistance was measured after each adhesion test.

In order to fabricate a surface dielectric barrier discharge plasma demonstrator, two different types of electrodes were placed between 1 mm thick glass substrates. The lower electrode was built using a Hi-Bond HB 720A Conductive Copper Tape (Hi-Bond, Korea) whereas the upper electrode was printed using the laser-induced scanning transfer method herein reported. High voltage alternating current was applied between

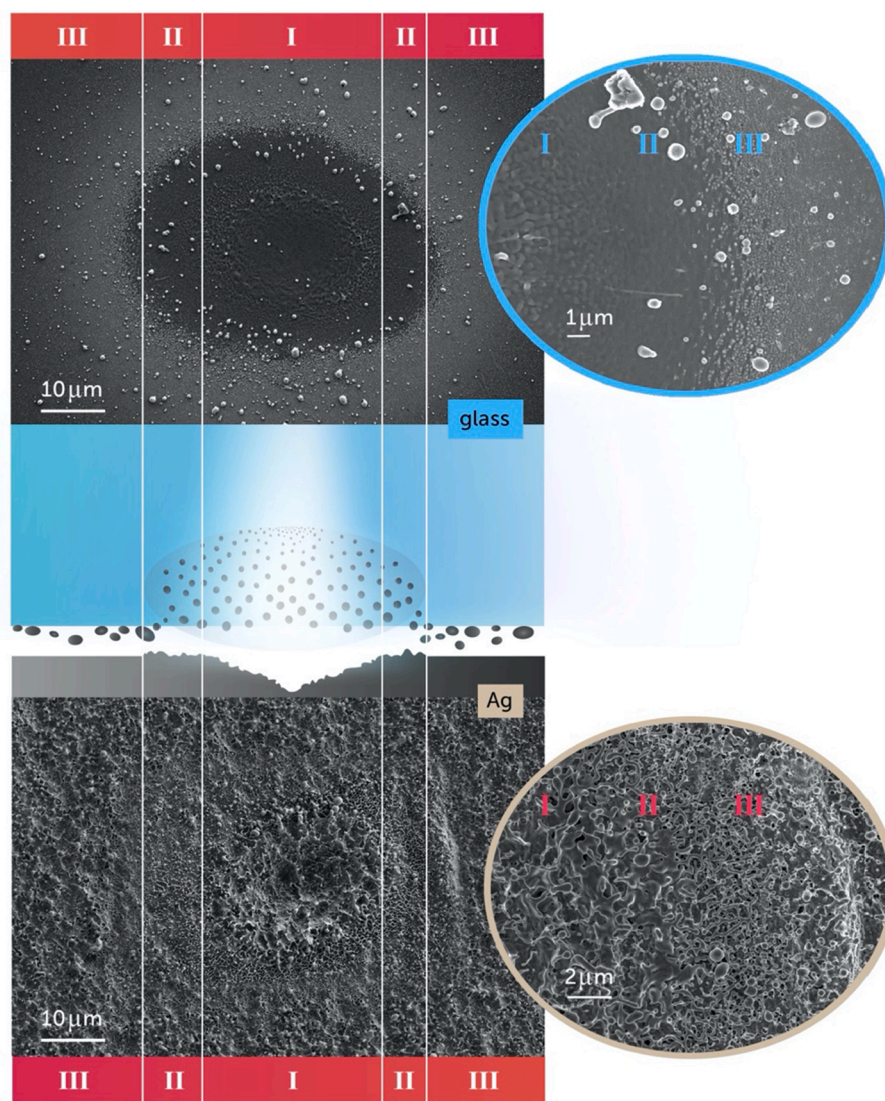


Fig. 2. Scheme of the Ag deposition on the glass during a laser pulse showing the three regions that have been identified. Aspect of the silver target (bottom part) and glass (upper part) surfaces after applying 100 pulses of energy $E_{\text{pulse}} = 4.36 \mu\text{J}$ (irradiance 1.89 GW/cm²) at a rate of 250 kHz. Top and bottom insets show plan-view images of the border of the target and glass spots displaying the three regions discussed in the text.

both electrodes. For this purpose, a 16-kHz AC signal was generated with a GF-855 function generator (Promax, Spain) connected to a linear amplifier AG-1012 (T&C Power Conversion, USA). A matching network and two transformers (HR-Diemen S.A., Spain) were also connected to the amplifier output to increase the output voltage up to approximately 20 kV peak-to-peak. The incident power in the surface dielectric barrier discharge plasma demonstrator was kept constant at 12 W.

3. Generation of the Ag coating

In an attempt to understand how Ag deposits on the glass substrate surface during LIRT, several experiments were initially carried out to obtain single spot or single line deposition. By combining the average laser power, P , and the pulse repetition frequency, f_p , it is possible to obtain defined values of the pulse energy E_{pulse} up to a maximum of 5.30 μJ . As the pulse width (300 ps) is constant in all these experiments, E_{pulse} is proportional to the irradiance. Taking into account that the laser beam profile is gaussian, it is important to consider both the average irradiance value, which considers the beam spot size defined with the $1/e^2$ criterium, and the peak value at the maximum of the gaussian, which is two times higher. In our case, these magnitudes approach values of 2.30 GW/cm^2 and 4.60 GW/cm^2 , respectively.

Fig. 2 contains an illustrative scheme of the ablation process triggered on a single incident spot upon irradiation, in burst mode, with 100 pulses of $E_{\text{pulse}} = 4.36 \mu\text{J}$ and 1.89 GW/cm^2 (average irradiance). The observed surface morphologies are shown for both, the silver target (bottom part) and the glass substrate (upper part). A different case, for 100 pulses of 2.12 μJ (0.92 GW/cm^2), is also presented in Fig. Sup2. In both cases, the corresponding irradiance peaks at the centre of the beam are above the target ablation threshold. Consequently, the focused laser pulses induce formation of craters on the Ag target, as well as material transfer effects to the glass substrate surface above, generating similar structures.

The spot sizes observed on the irradiated Ag and glass surfaces have, within experimental error, the same shapes, exhibiting three correlated regions that are clearly identified in Fig. 2. Because of the gaussian energy distribution in the laser beam, the silver target surface exhibits crater-like marks with higher erosion (depth) observed at the centre of the spot (region I). Spherical silver drops and a finer topography are observed on the adjacent area (region II), as a consequence of solidification of droplets ejected from the molten volume, consistent with a photothermally driven ablation mechanism [43]. Three distinct regions are also observed on the glass substrate just above, as identified within the upper inset in Fig. 2. Within region I, fine structures of nanoparticles seem to have penetrated inside the glass volume. Penetration of these structures inside the glass appears to decrease, however, within region II. Finally, in region III, the level of damage on the silver target surface appears to be very low, but it is in this region of the glass substrate where larger silver nanoparticles, which do not have enough energy to penetrate into the glass, are deposited on its surface. This is likely due to the mass ejection effects associated with the confined plasma plume shock waves generated during pulsed laser irradiation [44].

The spots observed on the silver target for the experiment carried out with $E_{\text{pulse}} = 2.12 \mu\text{J}$ (see Fig. Sup2) exhibit an elliptical shape with long axis $2a = 20 \mu\text{m}$ and short axis $2b = 17 \mu\text{m}$ (region I). In region II, these values change to $2a = 35 \mu\text{m}$ and $2b = 25 \mu\text{m}$. The width of region III ranges from 5 to 7 μm . When $E_{\text{pulse}} = 4.36 \mu\text{J}$ (see Fig. 2), the size of these different structures increases up to $2a = 30 \mu\text{m}$ and $2b = 18 \mu\text{m}$ for region I, $2a = 45 \mu\text{m}$ and $2b = 34 \mu\text{m}$ for region II and a width of 17 μm in region III within the glass, where the higher concentration of large nanoparticles is found in the central 3 μm zone.

In consequence, the first laser pulse produces an initial silver layer deposition on the glass substrate surface above, with two easily identifiable concentric regions in crown geometry. In the external region, large nanoparticles are deposited on the glass surface, while, in the inner one, small nanoparticles penetrate inside the glass. These observations

are consistent with a laser ablation nanoparticle generation mechanism based on Gaussian beam profiles, as proposed from molecular dynamics calculations and experimentally observed [42–47]. The highest absorption of energy during each pulse is produced at the centre of the target spot and the induced plasma absorption layer placed above is the most relevant. It is in this region where the onset of the gas plasma plume shock wave takes place, although it is very restricted here to the thickness of the air gap left between the target and the glass substrate. The main damage in the target and glass substrate is produced by the plasma shock waves, which in free conditions develop perpendicularly with maximum particle speed at its axis. The confinement of the plasma essentially to the volume defined by the air gap between the glass substrate and the target increases the radial expansion of the plasma at the edges of the substrate. Shock waves reflected by the target and, probably, successive echoes, would be responsible for the explosive projection of liquid droplets, rather than the direct shock waves associated to plasma formation [46]. Furthermore, spallation of the shallow regions of the target within the periphery leads to a process that involves peeling off continuous liquid layers. The latter exhibits a decrease in thickness as a function of distance to the spot centre. Speeds of the ejected nanoparticles and small nanoparticles from the centre of the laser beam can reach several thousands of $\text{m}\cdot\text{s}^{-1}$. Moving from the centre of the beam towards its periphery, their size increases at the same time that their speed decreases. In this case, the energy of the particles is not apparently sufficient to penetrate inside the glass, thus they deform when they impact the glass surface. Shock waves displace most of these particles to region III of the glass surface (Fig. 2).

The complex incubation effects associated to the multi-pulse irradiation of both, target and partially coated glass surface, make the overlap effects of consecutive pulses relevant for an effective control of the ablation process. Overlap within the beam scanning direction is determined by the distance between the beam spot centres of two successive pulses $\delta = v_L/f_p$, where v_L is the laser beam scanning speed. When the laser beam moves to the subsequent position, the laser must unavoidably pass through a portion of glass where silver nanoparticles are present inside or on its surface. This can produce the ejection of some Ag particles that were previously deposited on the glass substrate, resulting in a combination of LIRT and LIFT within the same area. In this process, shock waves also play an important role, moving most of the particles that are deposited on top of the glass surface. When the irradiance values are high enough, this LIFT-LIRT combination also induces projection of SiO_2 particles from the glass onto the Ag target, as confirmed by EDS measurements (see Fig. Sup3).

Taking into account these observations, a basic scheme is introduced in Fig. 3, where formation of the silver deposit on the glass substrate surface is illustrated as a combination of LIRT/LIFT/shock wave contributions from individual overlapping spots. Considering the high laser pulse repetition rates, the subsequent pulse partially overlaps with the previous one. Fig. 3a shows the scheme of a situation in which the second laser beam spot position reaches region III of the previous one. The black central part in each spot represents region I and II. Region III is represented with a lighter grey border. With these processing parameters, the laser beam fraction that strikes the previous LIRT deposit projects back some of the accumulated silver nanoparticles in region III onto the target, via a LIFT process.

To validate the proposed deposition scheme, several experiments were performed using only single laser beam scan lines. Fig. 3b shows the morphology of the glass surface of a single line deposited by the LIRT-LIFT processes previously outlined. The highest E_{pulse} value available for the laser source employed in this study (5.3 $\mu\text{J}/\text{pulse}$) was selected in order to obtain a noticeable coating with only a single pulse. The pulse repetition rate of 250 kHz and the scan velocity $v_L = 4000 \text{ mm}/\text{s}$ were chosen in order to maintain a δ value ($\delta = 16 \mu\text{m}$) larger than the thickness of region III. The experimentally observed surface morphology of chain-like links closely resembles the one predicted in the scheme. The results clearly show the combination of LIFT and LIRT

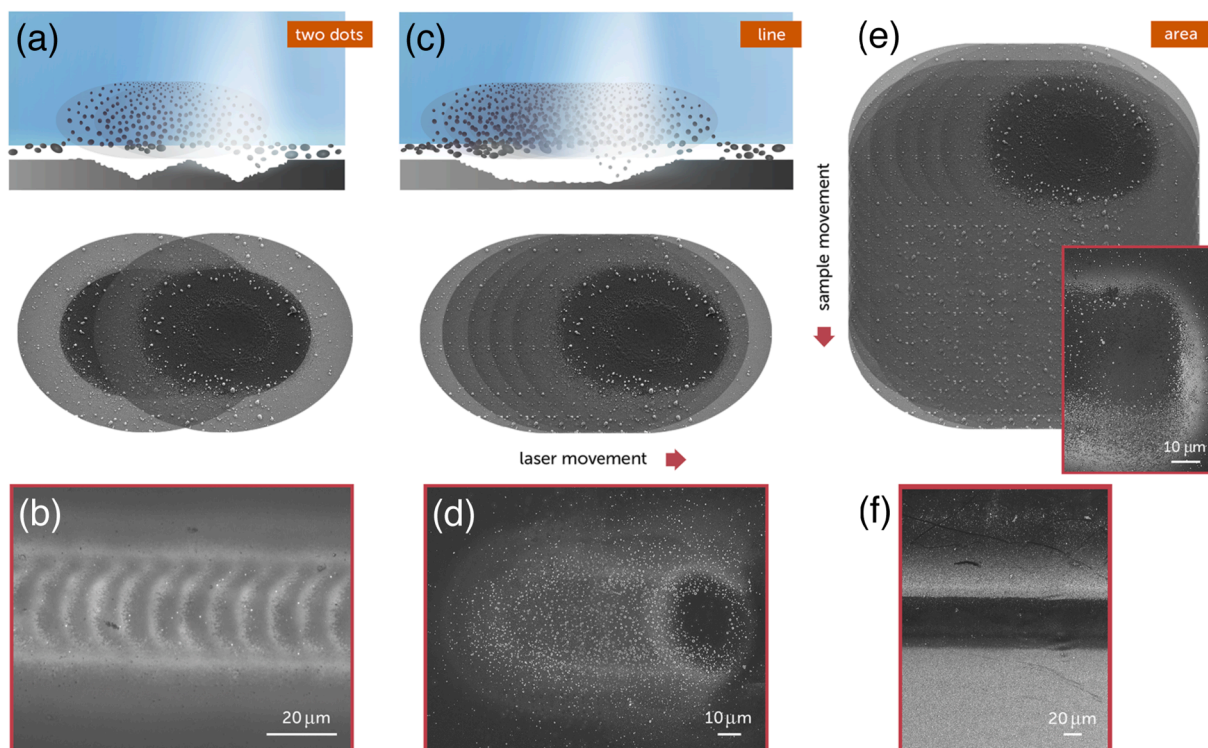


Fig. 3. Scheme of the combined LIRT-LIFT process proposed for the fabrication of Ag coatings on glass surfaces. (a) Scheme of the coating associated to two consecutive pulses when the laser in the second pulse reaches region III, generated in the first pulse. (b) Optical micrograph of a line generated using $f_p = 250$ kHz, $E_{\text{pulse}} = 5.3$ μJ , and $v_L = 4000$ mm/s. The distance between the centres of two pulse spots is $\delta = 16$ μm . (c) Scheme of the coating generation during a line scan. (d) Aspect of the beginning (left) and end (right) of the silver deposited on the glass after a single line with laser pulses of $E_{\text{pulse}} = 2.12$ μJ , $f_p = 400$ kHz and $v_L = 75$ mm/s ($\delta = 0.2$ μm). The arrow indicates the direction of the laser beam scan. (e) Scheme of the 2D coating generation indicating the sample movement direction. The inset shows a FESEM image of the end of ten overlapped laser scanned lines separated 2 μm using pulses of energy $E_{\text{pulse}} = 2.12$ μJ , $f_p = 400$ kHz and $v_L = 1125$ mm/s. (f) Aspect of the region close to the end of a 4 mm wide rectangle, processed applying the same laser parameters.

processes. With these experimental conditions, only the rear part of the structure generated by each individual pulse is observed, because the front part is destroyed by the coating associated with the subsequent pulse.

In order to have good electrical continuity along a line deposit, a continuous and thick Ag coating is needed. This requires a significant degree of overlap between consecutive pulses. When δ is lower than the width of region II, the LIFT process can take place with some of the nanoparticles that penetrate inside the glass, particularly with those near the glass outermost surface. Shock waves also push ahead the nanoparticles that are deposited on the glass surface, in the direction of the laser movement. These two LIRT-LIFT process combinations generate a Ag distribution similar to the one proposed in Fig. 3c. In the back side of the laser beam, the new Ag deposit on the surface overlaps with the initial one, yielding a thicker Ag layer on the glass substrate. In other areas, the silver deposited by ablation from the initial spot is now removed. The presented scheme illustrates the situation for which the distance between centres of two consecutive spots is $\approx 10\%$ of the single spot dimensions. Considering the size of the different regions presented in Fig. 2, under these experimental conditions, region I of the second spot does not reach region III of the previous spot. The laser beam thus has to travel through a portion of the glass where there are Ag nanoparticles embedded inside the glass. Due to the accumulative effects of several spots, the generated line would have three different band-like regions. The external, upper and lower parts in the line described by the laser accumulate a thicker Ag deposit, with a width approximately determined by that corresponding to the external crown generated by a single pulse. The central band of the line would accumulate lower amounts of Ag, with appreciable differences observable towards both, the beginning and the end of the line.

The image of Fig. 3d shows the beginning and end regions of a silver line deposited on the glass substrate with the following experimental conditions: $E_{\text{pulse}} = 2.12$ μJ , $f_p = 400$ kHz and $v_L = 75$ mm/s, leading to $\delta = 0.2$ μm and generating an overlap of approximately 99%. As predicted in the proposed LIFT-LIRT hypothetical deposition model, the beginning and end of the line are completely different.

Finally, to achieve 2D area coatings with good electrical continuity, the sample should move in the perpendicular direction to the laser beam scan during the fabrication process, as suggested in Fig. 3e and f. The last line projected by the laser appears on the upper side within the scheme presented in Fig. 3e. The latter predicts that the upper part of the previous line disappears via the movement of the Ag nanoparticles away from the incident laser line, due to interaction with shock waves, as well as via LIFT deposition onto the silver target again. As a consequence, the final silver coating on the glass surface is formed by the accumulation of silver that was projected towards the rear part of the different scanning lines described by the laser beam.

Moreover, the end of an area obtained by the overlap of 10 single pulse lines with 2 μm interline distance, is presented in the inset of Fig. 3e. Each individual line has been deposited using $E_{\text{pulse}} = 2.12$ μJ , $f_p = 400$ kHz, and $v_L = 1125$ mm/s, defining a distance between the centres of two consecutive spots as 2.8 μm . This FESEM image also shows the accumulation of Ag deposited on the rear part of the lines due to the movement of the sample. In addition, a FESEM image of the last part of a 4 mm-wide coating, obtained by applying the same experimental conditions, is presented in the Fig. 3f. It demonstrates that a uniform coating is obtained on the back-side of the laser line scan front.

These studies show the presence of two different coating structures. In the outer part of the coating, silver deposits are formed by nanoparticles originated in the solidification of molten material accumulated

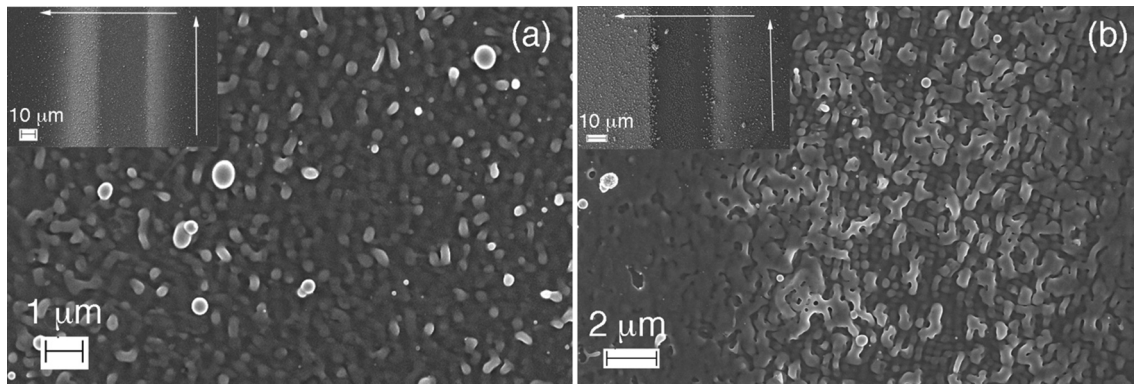


Fig. 4. FESEM planar-view images showing the detail of the structures in the centre of the last line scanned by the laser with $E_{\text{pulse}} = 1.71 \mu\text{J}$, $v_L = 1125 \text{ mm/s}$ and a distance between laser scanning lines of $2 \mu\text{m}$, after having processed $20 \mu\text{m}$ (a) or 4 mm (b). In the insets, a general overview of the aspect of this last line is presented in both cases. Vertical arrows show the direction of laser scanning, while horizontal ones indicate sample movement.

in the back-side of the laser front. However, a thorough analysis of the final part of the coating indicates the presence of a different structure in the centre of the last line scanned by the laser. This is the expected structure close to the glass surface. Fig. 4 shows this structure for a given processing condition at two different instants in the 2D coating process: at the beginning, after scanning only 10 lines and moving the sample $20 \mu\text{m}$, and at the end of the process, after having coated 4 mm in length. Observation of this deposit at the beginning of the process (Fig. 4a), suggests that it appears very similar to that observed in the centre of the spots in the initial experiments carried out in burst mode (Fig. 2). As a consequence, it can be deduced that structuring is strongly influenced by the nanoparticles with high energy that are generated at the centre of the laser spot and penetrate inside the glass. When the coating process evolves (Fig. 4b), the structure becomes planar with a threadlike morphology in the direction parallel to the glass surface.

4. Characterization of the Ag coating

4.1. Electrical resistance measurements

Results presented in the previous section suggest that the energy per pulse and the degree of overlap between different pulses are the parameters that control the quality of the Ag coating. Overlap in the beam scanning direction is determined by the ratio between $\delta = v_L/f_p$ and the beam dimensions at the target. The velocity of the target in the perpendicular direction controls the overlap of adjacent lines.

The performance of these coatings has been assessed by measuring the dc electrical resistances in 4 mm width rectangles using a four-point probe configuration. Initial experiments were performed modifying v_L , reaching the lowest DC resistance values with $f_p = 400 \text{ kHz}$ and $v_L = 1125 \text{ mm/s}$. With these parameters, $\delta = 2.8 \mu\text{m}$ and most of the laser beam crosses the glass through regions I and II (see Fig. 2) generated by the previous spot, without reaching region III. In addition, lower electric resistance values of 2D line arrangements have been obtained with a line overlap of $2.5 \mu\text{m}$, i.e., with similar degrees of overlap in both, beam scan and sample traverse directions. These processing parameters lead to a coating speed of $2.3 \text{ mm}^2/\text{s}$.

Considering these processing parameters, the effect of E_{pulse} was analysed and the results are presented in Fig. 5. Initially, a first series of experiments was followed for the sequence at 400 kHz and 1125 mm/s , varying E_{pulse} between $1.6 \mu\text{J}$ ($0.69 \text{ GW}/\text{cm}^2$) and $3.4 \mu\text{J}$ ($1.47 \text{ GW}/\text{cm}^2$) (green line). Measurements show that the electrical resistance varied more than five orders of magnitude as a function of the energy per pulse (average irradiance), reaching values $\approx 20 \Omega$ for $E_{\text{pulse}} = 3.3 \mu\text{J}$ ($1.43 \text{ GW}/\text{cm}^2$). In order to obtain data for higher E_{pulse} values, the pulse repetition frequency was reduced to 300 kHz at the same laser scan speed ($\delta = 3.75 \mu\text{m}$), exploring the range between $E_{\text{pulse}} = 2.5$ ($1.08 \text{ GW}/$

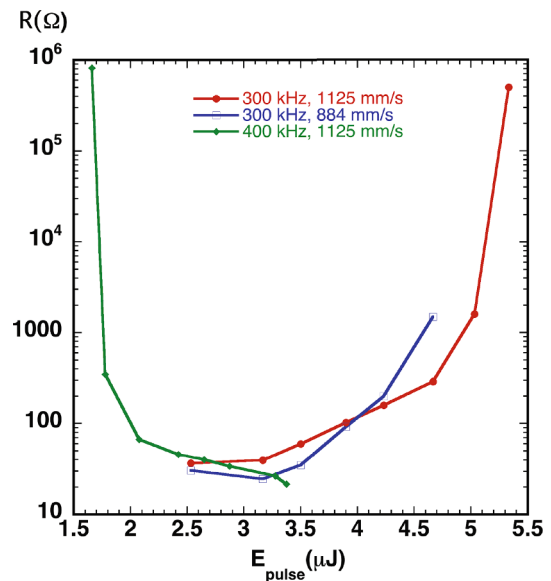


Fig. 5. Variation of the room temperature electrical resistance (measured on 3 mm length using the four-point probe method) as a function of E_{pulse} , for three different sets of laser frequency and laser scanning speed values. Coloured lines are just placed as eye-guides.

cm^2) and $5.3 \mu\text{J}$ ($2.30 \text{ GW}/\text{cm}^2$) in a second sequence of experiments (red line). The results yield a continuous and fast increase of the resistance as a function of E_{pulse} , and resistance values higher than those of samples produced at 400 kHz within the common $2.5 \mu\text{J} < E_{\text{pulse}} < 3.5 \mu\text{J}$ pulse energy range. Moreover, in order to clarify the relevance of the overlapping distance δ , a third series of experiments was carried out at 300 kHz while reducing v_L to 844 mm/s , conditions that lead again to $\delta = 2.8 \mu\text{m}$ (blue line). With these new conditions, the values of the resistance and the optimum E_{pulse} range are very similar to those obtained at 400 kHz . These results thus demonstrate the significant influence of both parameters, pulse energy E_{pulse} (irradiance) and pulse overlap (incubation), as well as their interdependence in order to achieve silver coatings with low electrical resistance.

Electrical resistance values have also been used as an indirect evidence of the adhesion quality of the metallic coating. Multiple scotch tape tests were performed in a number of representative samples, followed by electrical resistance evaluation. Fig. Sup4(a) and (b) show the aspect of a sample processed with $E_{\text{pulse}} = 4 \mu\text{J}$. This sample exhibited an electrical resistance value of 98Ω , which remained unaltered after the performance of six consecutive adhesion tests. As observed in Fig. Sup4 (c), the Ag particles that were deposited on the surface of the coating

were removed with the tape mainly during the first trial, leading to the conclusion that these particles are isolated, lose particles originated as debris during ablation, that do not contribute to the electrical performance of the coating.

4.2. Chemical state of silver deposits

The study of the composition and oxidation state of the different components at the surface was carried out by means of XPS. Three selected samples were chosen with the objective of addressing the different regimes observed in Fig. 5: Sample S1 was processed with $E_{\text{pulse}} = 1.66 \mu\text{J}$ (0.72 GW/cm^2), $f_p = 400 \text{ kHz}$ and $v_L = 1125 \text{ mm/s}$, S2 with $E_{\text{pulse}} = 3.27 \mu\text{J}$ (1.42 GW/cm^2), $f_p = 400 \text{ kHz}$ and $v_L = 1125 \text{ mm/s}$ very close to the optimum processing conditions that enable reaching the lowest resistance values, and S3 with the highest value of $E_{\text{pulse}} = 5.30 \mu\text{J}$ (2.30 GW/cm^2), $f_p = 300 \text{ kHz}$ and $v_L = 1125 \text{ mm/s}$. In the three samples, besides Ag, survey spectra reveal the presence of Si and Na signals (see Fig. Sup5), very likely because of the incorporation of glass particles in the coating due to the aforementioned combination of LIFT and LIRT processes. In addition, carbon and oxygen signals must be associated to carbonaceous species, and to partial oxidation of the Ag target and glass substrate deposit, respectively. Due to its relevance towards control of the conductivity properties of the films, particular attention was paid to the surface oxidation of silver. A proper determination of the chemical state of this element requires the analysis of both the Ag 3d photoemission and the Auger Ag MVV spectra (Fig. 6) and the determination of the Auger parameter derived from these values, according to:

$$\text{Auger Parameter } (\alpha) = \text{Binding Energy}_{(\text{Ag } 3d \text{ peak})} (\text{eV}) + \text{Kinetic Energy}_{(\text{Ag MVV})} (\text{eV})(1)$$

Binding energy and Auger parameter values deduced for the three samples are included in Table 1. The two α values reported for sample S3 stem from the two different features observable in the Auger spectra and support the fact that silver must be in this case deeply oxidized at the surface. In fact, α parameter values close to 726 eV are commonly associated to metallic silver, while values close to 723–725 eV are typical of oxidized silver [48]. According to this evaluation, silver is practically metallic in sample S1, some oxidation already occurs from sample S2 as revealed by the increase in the Auger parameter and the broadening of the Ag 3d peak, and a more evident oxidation occurs in sample S3 where silver oxide at the surface is likely to appear as a mixture of AgO and Ag₂O.

Therefore, the XPS analysis reveals that silver within the surface is

Table 1

Binding energy, Auger kinetic energy and Auger parameter measured in this work.

Sample	Binding energy (eV)	Auger kinetic energy (eV)	Auger parameter (eV)	State of oxidation
S1	367.9	358	725.9	Ag ⁺
S2	367.8	358	725.8	Ag ⁺
S3	367.2	355.8	723	AgO
		357.4	724.6	Ag ₂ O

metallic in sample S1, but it becomes partially oxidized as the energy per pulse is increased. This oxidation enhancement must contribute to increase the electrical resistance of the Ag deposit, because the building of an oxide layer at the surface hinders electron movement between silver grains.

4.3. Microstructural characterization

Sample S1 has a transparent aspect that indicates that the silver coating is rather thin and the amount of silver deposited on the glass is very low (see Fig. Sup6). This explains the high electrical resistance values measured in this sample. In order to complement XPS studies and attempt to understand why the resistance decreases nearly five orders of magnitude in the case of sample S2, while it increases for sample S3, a more detailed morphological study of the cross-sections was carried out for these two samples. FESEM images of the cross-sections of the coatings above the glass surfaces in both samples are presented in Fig. 7. In the case of sample S2 (Fig. 7a), the thickness of the coating ranges between 100 and 300 nm, and the size distribution of the Ag nanoparticulated grains is more uniform than in sample S3 (Fig. 7c). Moreover, the inset of Fig. 7c provides additional information to account for the higher electrical resistance of sample S3. Besides the higher degree of oxidation of the surface of this sample (c.f., Fig. 6), the inset shows that the Ag coating exhibits several grooves that reach the glass surface and, in consequence, contribute to break the metal film continuity. As a result, an increase in film resistance should be expected. Fig. 7a also shows that the adhesion of the Ag particles to the glass substrate in sample S2 must be quite effective, because it is observed that the nanoparticles that are close to the glass surface have partially penetrated inside it. This microstructure also explains the results obtained during the adhesion tests, discussed earlier.

To get a better insight about the sample in-depth microstructure, a TEM analysis was carried out on lamellas prepared from each sample. Results are presented in Fig. 7b, 7d, Sup7 and Sup8. In both cases, the Ag

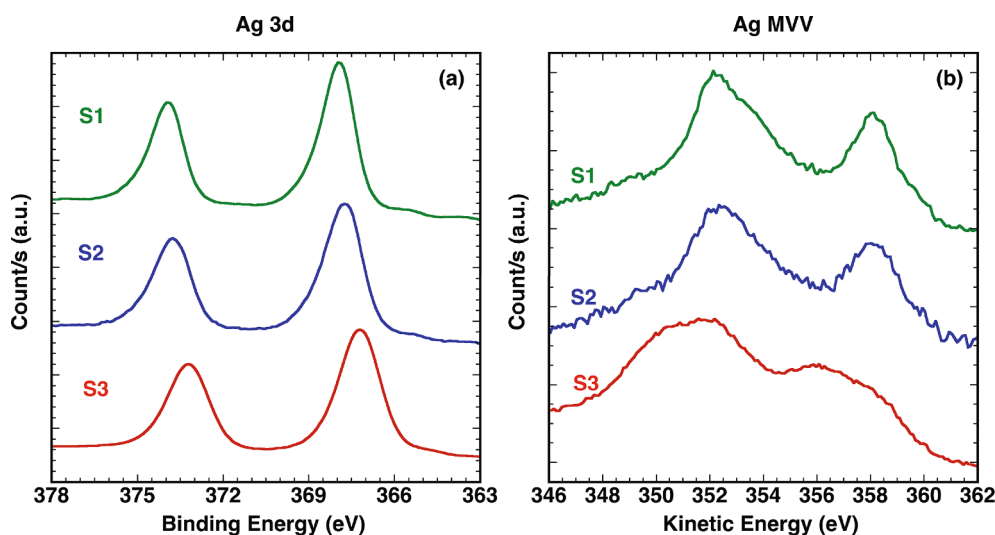


Fig. 6. (a) Normalized Ag 3d photoelectron, and (b) Ag MVV electron Auger spectra recorded for samples S1, S2 and S3.

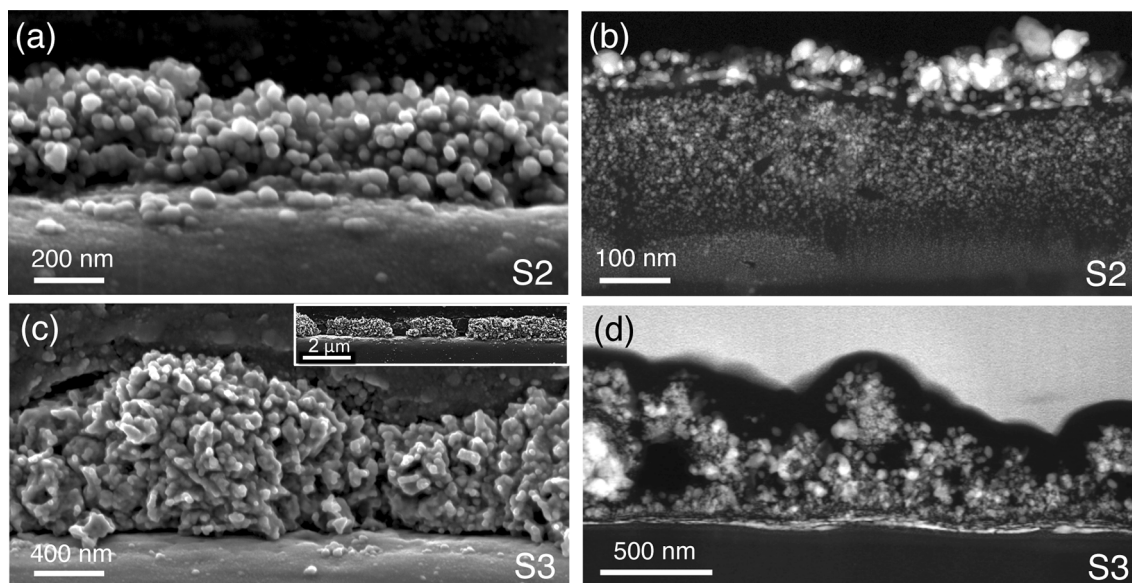


Fig. 7. FESEM and HAADF STEM images of the cross-sections of the coatings obtained in samples S2 (a and b, respectively) and S3 (c and d, respectively). The inset shows a larger region of the coating in the case of sample S3.

coatings exhibit some common trends. Two distinct regions could be identified above the glass surface. The Ag particles in contact with the glass surface appear elongated, depicting one single type of morphology in sample S2 and up to four in-depth layers in S3. It is convenient to recall here that this morphology was also observed when the surface of the final regions of the coatings were analysed by FESEM (Fig. 4). In contrast, within the most external parts of the Ag coating there appear more spherical nanoparticles. Their origin stems from the ejection of molten droplets during the mixed ablation mechanism to which the material has been subjected during sub-ns pulsed laser irradiation. It is also remarkable to observe that when E_{pulse} increases, the nanoparticle agglomeration density also increases, generating larger variations in the thickness of the coating, with values ranging between 330 and 830 nm.

In addition, TEM micrographs demonstrate that a fraction of Ag nanoparticles has penetrated inside the glass. In the case of sample S2 (Fig. 7b and Sup7) four different regions may be identified. Within the first region, near the outermost surface of the glass, some particles with diameters between 8 and 40 nm exhibit two grey contrasts. This could mean that they have penetrated partially on the glass, as deduced from Fig. 7a, improving the adhesion with the substrate. The second region, just below and away from the glass surface, appears with a thickness ranging between 170 and 310 nm. It appears to contain an accumulation of spherical nanoparticles with sizes between 3 and 10 nm. Smaller particles (1–3 nm) with higher kinetic energy, projected during the ablation process, penetrate further inside the glass and yield a third observable region with a thickness between 30 and 90 nm (Fig. 7c). Finally, the innermost part of the coating contains a fourth region with even smaller particles, observed with sizes smaller than 1 nm.

In the case of sample S3 (Figs. 7d and Sup8), it seems that the observed dense layers of flattened particles, deposited on the glass surface, block additional Ag particles from penetrating inside the glass. In this sample, only two regions of nanoparticles are thus distinguished inside the glass substrate. Their size is reduced to diameters ranging between 0.8 and 2 nm.

Electron diffraction studies have also been performed in a number of the particles from both of the above samples (Fig. Sup9). In both cases, the reflections obtained correspond to metallic fcc Ag, indicating that the amount of oxidation during the LIRT process is very limited or non-detectable under these observation conditions. This correlates with EDS measurements taken in the region with nanoparticles and inside the

glass, as can be observed in Fig. Sup10. In some cases, some traces of silver oxide are also detected, as confirmed in the corresponding XPS analysis presented in the previous section.

5. DBD demonstrator

The possibilities for applications offered by the silver deposits prepared on glass by this laser technology have been proven in a demanding application requiring a high conductivity and, simultaneously, high stability under rather aggressive operational conditions. Namely, as a proof-of-principle, the possibility of building surface interdigital electrical connections for the development of a surface dielectric barrier discharge (DBD) demonstrator was explored. The suitability of the deposition methodology for large area applications is an additional factor justifying this test.

A laboratory scale example is presented in Fig. 8. In this example, a DBD plasma is generated at the surface of a glass plate acting as dielectric material and decorated on one side with conductive silver threads deposited by LIRT as reported in this work and, on the other, by copper tape electrodes for simplicity. Typical dimensions, separation, etc. of the finger electrodes are indicated in Fig. 8(a) and (b). A typical surface DBD plasma actuator usually integrates two flat interdigitated electrodes mounted on both sides of a dielectric plate (1 mm thick glass) [49,50]. Plasma is generated on the dielectric areas among the electrodes when a sufficiently high voltage is applied between the electrodes to ionize the surrounding air (discharges typically occur in the range from few kV to 50 kV, depending on the electrode layout and other variables) [35]. Such an electrode configuration has been constructed by different methods. For example, using mesh wire electrodes mounted on an insulating plate with the second sheet electrode below the plate [41], by printing structured metal films on the insulating plates or by selective etching of circuit boards [40,42,51]. Fig. 8(c) and (d) show the aspect of the demonstrator without applying the voltage and during operation. Plasma generation is very uniform throughout the circuit, demonstrating that its electrical characteristics exhibit a high degree of uniformity. The robust and long-term operation of the device, demonstrated in this work for several hours under steady state conditions, proved the feasibility of the processing method for the preparation of highly conductive electrodes and its compatibility with large area applications in aggressive media, as those existing in a plasma.

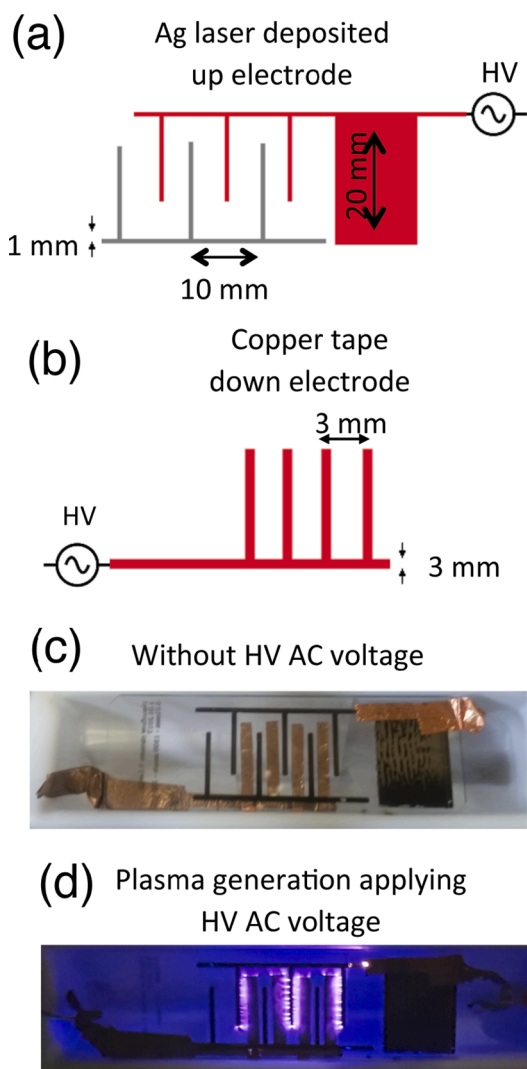


Fig. 8. (a) and (b) schematics of the up and down electrodes mounted between the glass substrate (1 mm thick). The horizontal distance between upper and lower electrodes is 1 mm. The Ag deposited electrode, coloured in grey in the upper part, was not connected to HV AC voltage in this experiment. (c) Surface dielectric barrier discharge (DBD) demonstrator in the absence of HV AC voltage and (d) after having applied a HV AC voltage (20 kV, 16 kHz, 12 W).

6. Conclusions

The study of the LIRT generation of Ag coatings on a glass surface using a 300 ps UV pulsed laser with high repetition rates has demonstrated the importance of the laser irradiance values, as well as the overlap between consecutive laser pulses, to obtain a metallic layer with desired electrical resistance values for a number of foreseen applications. It has been observed that the electrical characteristics of the coatings are very sensitive to the laser emission parameters, yielding values of electrical resistivity that differ in nearly five orders of magnitude.

Pulse to pulse overlap, intrinsic to this method, generates a combination of LIFT and LIRT phenomena that is responsible for the microstructures observed on the coatings. These result from the different kinds of nanoparticles integrated within the coatings and their relation with the different kinetic energies and nanoparticle sizes that are intrinsic to the applied sub-ns ablation process. Two metal coating layers are formed on the outermost surface of the glass substrate. A layer (Ag) with a planar structure is observed immediately adjacent and in contact to the glass surface. Images show efficient Ag grain connectivity within this

part of the coating. On the surface of this Ag coating, however, large accumulations of larger size Ag nanoparticles appear. In contrast, different layers of Ag nanoparticles are identified inside the glass substrate in the vicinity of the coating. This suggests that smaller nanoparticles are ejected through the ablation plume at higher kinetic energies when they are formed, and can penetrate further inside the glass.

When low irradiance or E_{pulse} values are used, the amount of silver deposited on top of the glass is too low to reach a minimum electrical conductivity. On the contrary, when excessively high E_{pulse} values are used, the coating exhibits cracks, the extent of oxidation of the external Ag particles is higher and the electrical resistance of the metallic deposit increases. Under optimum laser conditions, the coating exhibits a rather uniform structure and good adherence between particles, as well as with the glass substrate surface. This was confirmed with scotch tape adhesion tests, where electrical resistance values remain constant even after six successive test runs. Only the Ag particles that are loosely deposited on the external part of the coating are removed by the scotch tape and they do not contribute to the electrical conductivity. The above laser processing conditions have been chosen to build a DBD plasma demonstrator, showing the practical potential of this simple, non-expensive and environmentally advantageous technique.

CRediT authorship contribution statement

R. Molina: Conceptualization, Investigation, Writing - review & editing. **M. Ertuğrul:** Investigation. **A. Larrea:** Investigation, Formal analysis, Writing - review & editing, Visualization. **R. Navarro:** Conceptualization, Writing - review & editing. **V. Rico:** Investigation, Resources, Writing - review & editing. **F. Yubero:** Investigation, Writing - review & editing, Funding acquisition. **A.R. González-Elipe:** Investigation, Formal analysis, Writing - review & editing. **G.F. de la Fuente:** Conceptualization, Methodology, Writing - review & editing, Funding acquisition. **L.A. Angurel:** Conceptualization, Methodology, Investigation, Writing - original draft, Visualization, Funding acquisition.

Declaration of Competing Interest

The authors declare that they have no known competing financial interests or personal relationships that could have appeared to influence the work reported in this paper.

Acknowledgements

This paper is dedicated to the memory of Prof. Rafael Navarro. The authors gratefully acknowledge the financial support from Spanish MINECO-AEI and EU FEDER Program (projects ENE2017-83669-C4-1-R and MAT2016-79866-R), from EU project SPRINT (H2020-FETOPEN 801464) and from the Gobierno de Aragón “Construyendo Europa desde Aragón” (research group T54_20R). Authors also would like to acknowledge the use of Servicio General de Apoyo a la Investigación-SAI and the National Facility ELECMI ICTS, node “Laboratorio de Microscopías Avanzadas” at University of Zaragoza.

Appendix A. Supplementary material

Supplementary data to this article can be found online at <https://doi.org/10.1016/j.apsusc.2021.149673>.

References

- [1] D.M. Mattox, Handbook of Physical Vapor Deposition (PVD), in: Processing, 2nd Edition., Elsevier Inc, Oxford, UK, 2010, <https://doi.org/10.1016/C2009-0-18800-1>.
- [2] C.J. Brinker, A.J. Hurd, P.R. Schunk, G.C. Frye, C.S. Ashley, Review of sol-gel thin film formation, *J. Non-Crystalline Solids* 147–148 (1992) 424–436, [https://doi.org/10.1016/S0022-3093\(05\)80653-2](https://doi.org/10.1016/S0022-3093(05)80653-2).

- [3] N. Sahu, B. Parija, S. Panigrahi, Fundamental understanding and modeling of spin coating process: A review, *Indian J. Phys.* 83 (4) (2009) 493–502, <https://doi.org/10.1007/s12648-009-0009-z>.
- [4] K. Knoth, S. Engel, C. Apetriu, M. Falter, B. Schlobach, R. Hühne, S. Oswald, L. Schultz, B. Holzapfel, Chemical solution deposition of $\text{YBa}_2\text{Cu}_3\text{O}_{7-x}$ coated conductors, *Curr. Opin. Solid State Mater. Sci.* 10 (5-6) (2006) 205–216, <https://doi.org/10.1016/j.cossms.2007.07.001>.
- [5] C.E.J. Cordonier, K. Okabe, Y. Horiuchi, A. Nakamura, K. Ishikawa, S. Seino, S. Takagi, H. Honma, Formation of micrometer scale metal structures on glass by selective electroless plating on photopatterned titanium and copper containing films, *Langmuir* 33 (51) (2017) 14571–14579, <https://doi.org/10.1021/acs.langmuir.7b03329>.
- [6] P. Benajamin, C. Weaver, The adhesion of evaporated metal films on glass, *Proc. Royal Soc. London. Series A. Math. Phys. Sci.* 261 (1961) 516–531, <https://doi.org/10.1098/rspa.1961.0093>.
- [7] K. Prajwal, G.L. Priyanka, M.A. Hasan, A. Carmel Mary Esther, N. Sridhara, A. Rajendra, S.B. Arya, A. Dey, Development of reflective co-sputtered nanostructured metallic films, *Surf. Eng.* 37 (3) (2021) 400–405, <https://doi.org/10.1080/02670844.2020.1781376>.
- [8] P.J. Martin, A. Bendavid, T.J. Kinder, Control of film properties during filtered arc deposition, *Surf. Coat. Technol.* 81 (1) (1996) 36–41, [https://doi.org/10.1016/0257-8972\(95\)02530-8](https://doi.org/10.1016/0257-8972(95)02530-8).
- [9] D.M. Mattox, Ion plating—past, present and future, *Surf. Coat. Technol.* 133 (134) (2000) 517–521, [https://doi.org/10.1016/S0257-8972\(00\)00922-1](https://doi.org/10.1016/S0257-8972(00)00922-1).
- [10] D.B. Chrisey, G.K. Hubler, Pulsed Laser Deposition of Thin Films, John Wiley & Sons Inc, New York, 1994.
- [11] D. Fischer, G.F. de la Fuente, M. Jansen, A new pulsed laser deposition technique: Scanning multi component pulsed laser deposition method, *Rev. Sci. Instrum.* 83 (4) (2012) 043901, <https://doi.org/10.1063/1.3697861>.
- [12] J. Hämäläinen, M. Ritala, M. Leskelä, Atomic layer deposition of noble metals and their oxides, *Chem. Mater.* 26 (1) (2014) 786–801, <https://doi.org/10.1021/cm402221y>.
- [13] D. Muñoz-Rojas, T. Maindrón, A. Esteve, F. Pierrat, J.C.S. Kools, J.-M. Decams, Speeding up the unique assets of atomic layer deposition, *Mater. Today Chem.* 12 (2019) 96–120, <https://doi.org/10.1016/j.mtchem.2018.11.013>.
- [14] W. Zhou, S. Bai, Y. Ma, D. Ma, T. Hou, X. Shi, A. Hu, Laser-direct writing of silver metal electrodes on transparent flexible substrates with high-bonding strength, *ACS Appl. Mater. Interfaces* 8 (37) (2016) 24887–24892, <https://doi.org/10.1021/acsami.6b07696>.
- [15] J. Zhang, J. Feng, L. Jia, H. Zhang, G. Zhang, S. Sun, T. Zhou, Laser-induced selective metallization on polymer substrates using organocopper for portable electronics, *ACS Appl. Mater. Interfaces* 11 (14) (2019) 13714–13723, <https://doi.org/10.1021/acsami.9b01856>.
- [16] F. Zhao, C. Jiao, D. Xie, B. Lu, M. Qiu, X. Yi, J. Liu, C. Wang, L. Shen, Z. Tian, Research on laser-assisted selective metallization of a 3D printed ceramic surface, *RSC Adv.* 10 (72) (2020) 44015–44024, <https://doi.org/10.1039/D0RA08499A>.
- [17] J. Bohandy, B.F. Kim, F.J. Adrian, Metal deposition from a supported metal film using an excimer laser, *J. Appl. Phys.* 60 (4) (1986) 1538–1539, <https://doi.org/10.1063/1.337287>.
- [18] V.P. Veiko, E.A. Shakhno, V.N. Smirnov, A.M. Miaskovskiy, G.D. Nikishin, Laser-induced film deposition by LIFT: Physical mechanisms and applications, *Laser Part. Beams* 24 (2) (2006) 203–209, <https://doi.org/10.1017/S0263034606060289>.
- [19] P. Serra, A. Piqué, Laser-induced forward transfer: fundamentals and applications, *Adv. Mater. Technol.* 4 (1) (2019) 1800099, <https://doi.org/10.1002/admt.v4.110.1002/admt.201800099>.
- [20] Y. Shan, X. Zhang, H. Li, Z. Zhan, Single-step printing of high-resolution, high-aspect ratio silver lines through laser-induced forward transfer, *Optics Laser Technol.* 133 (2021) 106514, <https://doi.org/10.1016/j.optlastec.2020.106514>.
- [21] S. Xu, L. Ren, B. Liu, J. Wang, B. Tang, W. Zhou, L. Jiang, Single-step selective metallization on insulating substrates by laser-induced molten transfer, *Appl. Surf. Sci.* 454 (2018) 16–22, <https://doi.org/10.1016/j.apsusc.2018.05.144>.
- [22] S. Surdo, A. Diaspro, M. Duocastella, Printability conditions for an all-solid-state laser transfer, *Appl. Surf. Sci.* 506 (2020) 144969, <https://doi.org/10.1016/j.apsusc.2019.144969>.
- [23] A. Orera Utrilla, Glass Metallization via Laser Ablation Techniques. Engineering Thesis, University of Zaragoza, 2002.
- [24] R. Rangel-Rojo, A. Castelo, C. Gómez-Reino, C.I. López-Gascón, G.F. de la Fuente, Refractive index modification in glass by laser backwriting ablation of metals, *Opt. Exp.* 14 (2006) 8765–8771, <https://doi.org/10.1364/OE.14.008765>.
- [25] A. Castelo, D. Nieto, C. Bao, M.T. Flores-Arias, M.V. Pérez, C. Gómez-Reino, C. López-Gascón, G.F. de la Fuente, Laser backwriting process on glass via ablation of metal targets, *Opt. Commun.* 273 (1) (2007) 193–199, <https://doi.org/10.1016/j.optcom.2006.12.005>.
- [26] F. Rey-García, M.T. Flores-Arias, C. Gómez-Reino, R. Lahoz, G.F. de la Fuente, W. Assenmacher, W. Mader, Microstructure of planar glass substrates modified by Laser Ablation Backwriting (LAB) of metal targets, *Appl. Surf. Sci.* 307 (2014) 645–653, <https://doi.org/10.1016/j.apsusc.2014.04.091>.
- [27] G. Dhani, B. Tan, K. Venketakrishnan, Laser induced reverse transfer of gold thin films using femtosecond laser, *Opt. Lasers Eng.* 49 (2011) 866–869, <https://doi.org/10.1016/j.optlaseng.2011.02.019>.
- [28] P. Papakonstantinou, N.A. Vainos, C. Fotakis, Fabrication by UV femtosecond laser ablation of Pt, Cr and indium oxide thin films, *Appl. Surf. Sci.* 151 (1999) 159–170, [https://doi.org/10.1016/S0169-4332\(99\)00299-8](https://doi.org/10.1016/S0169-4332(99)00299-8).
- [29] D.J. Wu, M.H. Hong, R. Ji, K.D. Ye, S.M. Huang, T.C. Chong, T.C. Ma, K. Sugioka, K. Midorikawa, Laser Induced Diffusion for Glass Metallization, *Proceedings of SPIE Vol. 5063 Fourth International Symposium on Laser Precision Microfabrication*, edited by Isamu Miyamoto, Andreas Ostendorf, Koji Sugioka, Henry Helvajian, (SPIE, Bellingham, WA, 2003).
- [30] M.T. Flores-Arias, A. Castelo, C. Gomez-Reino, G.F. de la Fuente, Phase diffractive optical gratings on glass substrates by laser ablation, *Opt. Commun.* 282 (6) (2009) 1175–1178, <https://doi.org/10.1016/j.optcom.2008.11.067>.
- [31] M. Flury, C. Pédri, Laser induced reverse transfer with metal and hybrid material prepared with sol-gel process used on glass substrate, *Appl. Surf. Sci.* 278 (2013) 142–145, <https://doi.org/10.1016/j.apsusc.2012.11.071>.
- [32] Jichao Zhang, Faze Chen, Yao Lu, Zhongtao Zhang, Jiuyu Liu, Yang Chen, Xin Liu, Xiaolong Yang, Claire J. Carmalt, Ivan P. Parkin, Superhydrophilic-superhydrophobic patterned surfaces on glass substrate for water harvesting, *J. Mater. Sci.* 55 (2) (2020) 498–508, <https://doi.org/10.1007/s10853-019-04046-x>.
- [33] N. Safaie, H. Jones-Taggart, A. Kiani, High intensity laser induced reverse transfer: Solution for enhancement of biocompatibility of transparent biomaterials, *Coatings* 9 (2019) 586, <https://doi.org/10.3390/coatings9090586>.
- [34] R. Brandenburg, Dielectric barrier discharges: progress on plasma sources and on the understanding of regimes and single filaments, *Plasma Sources Sci. Technol.* 26 (2017) 53001, <https://doi.org/10.1088/1361-6595/aa6426>.
- [35] J.J. Wang, K.S. Choi, L.H. Feng, T.N. Jukes, R.D. Whalley, Recent developments in DBD plasma flow control, *Prog. Aerosp. Sci.* 62 (2013) 52–78, <https://doi.org/10.1016/j.paerosci.2013.05.003>.
- [36] M.A. Malik, K.H. Schoenbach, R. Heller, Coupled surface dielectric barrier discharge reactor-ozone synthesis and nitric oxide conversion from air, *Chem. Eng. J.* 256 (2014) 222–229, <https://doi.org/10.1016/j.cej.2014.07.003>.
- [37] Y. Bellebna, A. Tilmatine, Application of dielectric Surface barrier discharge for air disinfection, *Acta Electro. Inform.* 13 (2013) 22–26, <https://doi.org/10.2478/aei-2013-0035>.
- [38] L. Černáková, D. Kováčik, A. Zahoranová, M. Černák, M. Mazúr, Surface modification of polypropylene non-woven fabrics by atmospheric-pressure plasma activation followed by acrylic acid grafting, *Plasma Chem. Plasma Process.* 25 (4) (2005) 427–437, <https://doi.org/10.1007/s11090-004-3137-4>.
- [39] S. Shimizu, S. Barczyk, P. Rettberg, T. Shimizu, T. Klampff, J.L. Zimmermann, T. Hoeschen, C. Linsmeier, P. Weber, G.E. Morfill, H.M. Thomas, Cold atmospheric plasma - A new technology for spacecraft component decontamination, *Planet Space Sci.* 90 (2014) 60–71, <https://doi.org/10.1016/j.pss.2013.10.008>.
- [40] G.E. Morfill, T. Shimizu, B. Steffes, H-U. Schmidt, Nosocomial infections - a new approach towards preventive medicine using plasmas, *New J. Phys.* 11 (11) (2009) 115019, <https://doi.org/10.1088/1367-2630/11/11/115019>.
- [41] M. Hähnel, T. von Woedtke, K.D. Weltmann, Influence of the air humidity on the reduction of bacillus spores in a defined environment at atmospheric pressure using a dielectric barrier surface discharge, *Plasma Process Polym.* 7 (2010) 244–249, <https://doi.org/10.1002/ppap.200900076>.
- [42] V. Lennikov, B. Özkurt, L.A. Angurel, A. Sotelo, B. Özçelik, G.F. de la Fuente, Microstructure and transport properties of Bi-2212 prepared by CO₂ laser line scanning, *J. Supercond. Nov. Magn.* 26 (4) (2013) 947–952, <https://doi.org/10.1007/s10948-012-1934-1>.
- [43] G. Cristoforetti, S. Legnaioli, V. Pallechi, E. Tognoni, P.A. Benedetti, Observation of different mass removal regimes during the laser ablation of an aluminium target in air, *J. Anal. At. Spectrom.* 23 (2008) 1518–1528, <https://doi.org/10.1039/B800517F>.
- [44] Maxim V. Shugaev, Chengping Wu, Oskar Armbruster, Aida Naghilou, Nils Brouwer, Dmitry S. Ivanov, Thibault J.-Y. Derrien, Nadezhda M. Bulgakova, Wolfgang Kautek, Baerbel Rethfeld, Leonid V. Zhigilei, Fundamentals of ultrafast laser-material interaction, *MRS Bull.* 41 (12) (2016) 960–968, <https://doi.org/10.1557/mrs.2016.274>.
- [45] Chengping Wu, Leonid V. Zhigilei, Microscopic mechanisms of laser spallation and ablation of metal targets from large-scale molecular dynamics simulations, *Appl. Phys. A* 114 (1) (2014) 11–32, <https://doi.org/10.1007/s00339-013-8086-4>.
- [46] Eaman T. Karim, Maxim Shugaev, Chengping Wu, Zhibin Lin, Robert F. Hainsey, Leonid V. Zhigilei, Atomistic simulation study of short pulse laser interactions with a metal target under conditions of spatial confinement by a transparent overlayer, *J. Appl. Phys.* 115 (18) (2014) 183501, <https://doi.org/10.1063/1.4872245>.
- [47] C.Y. Shih, R. Streubel, J. Heberle, A. Letzel, M.V. Shugaev, C. Wu, M. Schmidt, B. Göckel, S. Barcikowski, L.V. Zhigilei, Two mechanism of nanoparticle generation in picosecond laser ablation in liquids: the origin of the bimodal size distribution, *Nanoscale* 10 (2018) 6900–6910, <https://doi.org/10.1039/c7nr08614h>.
- [48] Santanu Bera, P. Gangopadhyay, K.G.M. Nair, B.K. Panigrahi, S.V. Narasimhan, Electron spectroscopic analysis of silver nanoparticles in a soda-glass matrix, *J. Electron Spectrosc. Relat. Phenom.* 152 (1-2) (2006) 91–95, <https://doi.org/10.1016/j.elspec.2006.03.008>.
- [49] J. Jolibois, N. Zouzou, E. Moreau, J.M. Tabibouët, Generation of surface DBD on rough dielectric: Electrical properties, discharge-induced electric wind and generated chemical species, *J. Electrostat.* 69 (6) (2011) 522–528, <https://doi.org/10.1016/j.elstat.2011.07.001>.
- [50] N. Benard, E. Moreau, Electrical and mechanical characteristics of surface AC dielectric barrier discharge plasma actuators applied to airflow control, *Exp. Fluids* 2014 (1846) 55, <https://doi.org/10.1007/s00348-014-1846-x>.
- [51] Marcel Hähnel, Volker Brüser, Holger Kersten, Diagnostics of SiO_x-containing layers deposited on powder particles by dielectric barrier discharge, *Plasma Process Polym.* 4 (6) (2007) 629–637, <https://doi.org/10.1002/ppap.200700015>.